

General Time-Dependent Configuration-Interaction Singles II: The Atomic Case

Stefanos Carlström ^{1,2,*} Mattias Bertolino ² Jan Marcus Dahlström ² and Serguei Patchkovskii¹

¹*Max-Born-Institut, Max-Born-Straße 2A, 12489 Berlin, Germany*

²*Department of Physics, Lund University, Box 118, SE-221 00 Lund, Sweden*

(Dated: September 7, 2022)

We present a specialization of the grid-based implementation of the time-dependent configuration-interaction singles described in the preceding paper [1] to the case of spherical symmetry. We describe the intricate time propagator in detail, and conclude with a few example calculations. Among these, of note are high-resolution photoelectron spectra in the vicinity of the Fano resonances in photoionization of neon, and spin-polarized photoelectrons from xenon, in agreement with recent experiments.

Keywords: Schrödinger equation, time-dependent configuration-interaction singles, photoelectron spectra, strong-field dynamics, spin-orbit dynamics, two-component quasi-relativistic

II.1. INTRODUCTION

This article describes the specialization of the general time-dependent configuration-interaction singles presented in the preceding article [1, hereinafter referred to as I] to the atomic case, taking advantage of the spherical symmetry of the field-free Hamiltonian. Where previously, the particle orbitals only had two components, spin-up and spin-down ($\alpha, \beta \equiv m_s = \pm 1/2$) respectively, they are now expanded in spherical harmonics as well ($n\ell m_\ell m_s$ basis), or directly in two-component spinor spherical harmonics [$n\ell j m_j$ basis; see section 7.2 of 2]. The two-component formulation allows us to treat spin-dependent effects *ab initio*, an important advance beyond previous work [3–5]. Since the spin-angular algebra is fully analytic, the numerics are reduced to coupled one-dimensional radial problems, which although constituting a more compact basis than the three-dimensional Cartesian grids used in the general case, also leads to comparatively more involved expressions. The spectral properties of the matrix representations of the various terms of the Hamiltonian also change, which requires additional care when designing the time propagation scheme.

This article is arranged as follows: in section II.2, the atomic structure problem is briefly surveyed, section II.3, which constitutes the bulk of the paper, describes the details of the time propagation scheme, and section II.4 illustrates the implementation with some example calculations. Finally, section II.5 concludes the paper. The same notation and conventions are used as detailed in I.1 A. The atomic unit of time is 1 jiffy ≈ 24.2 as, as introduced by Harriman [6].

II.2. ATOMIC STRUCTURE

In contrast to the general case I, in the atomic case the Hartree–Fock (HF) problem is solved on the same grid used to resolve the particle orbitals $|\tilde{k}\rangle, |\tilde{l}\rangle, \dots$. Furthermore, we also require that the reference state is a solution to the HF equations, instead of a general determinant. As a result, the matrix representation of the \hat{f} operator is diagonal in the space spanned by occupied orbitals, which simplifies the equations of motion (EOMs).

The Hamiltonian we consider is the following

$$\begin{aligned} \hat{H}(t) &= \hat{h}_i + \hat{g}_{ij} + \hat{V}_{L;i}(t) \\ &= \frac{p_i^2}{2} + \frac{\ell(\ell+1)}{2r_i^2} + V_C(r_i) + V_{\text{CAP}}(r_i) + \frac{1}{2r_{ij}} \\ &\quad + \begin{cases} \mathbf{F}(t) \cdot \mathbf{r}_i, & \text{(length gauge),} \\ \mathbf{A}(t) \cdot \mathbf{p}_i + \hat{\mathbf{1}}_i \frac{A^2(t)}{2}, & \text{(velocity gauge),} \end{cases} \end{aligned} \quad (\text{II-1})$$

where \hat{h} is the one-body Hamiltonian, \hat{g} is the two-body Coulomb electron–electron repulsion interaction [the term $(2r_{ii})^{-1}$ is excluded from the summation], and $\hat{V}_L(t)$ is the time-dependent interaction with an external field. Each term will be described in more detail below. See appendix A for a brief description of the discretization of the radial problem.

A. Relativistic effective core potentials

Although the EOMs (I-5†) are not spin-restricted, they would yield the same result as a one-component calculation, i.e. there would be no effect due to the spin of the electrons. To implement spin-orbit coupling (and other vector-relativistic effects), account for scalar-relativistic effects, and at the same time reduce the number of electrons we need to explicitly treat in the calculation, we replace V_C in (II-1) by a relativistic effective-core potential (RECP), which models the nucleus and

* stefanos@mbi-berlin.de; stefanos.carlstrom@matfys.lth.se

the core electrons according to

$$\hat{V}_{\text{RECP}}(\mathbf{r}) = -\frac{Q}{r} + B_{\ell_j}^k \exp(-\beta_{\ell_j}^k r^2) \hat{P}_{\ell_j},$$

where Q is the residual charge, \hat{P}_{ℓ_j} is a projector on the spin–angular symmetry ℓ_j , and $B_{\ell_j}^k$ and $\beta_{\ell_j}^k$ are numeric coefficients found by fitting to excited spectra computed using multiconfigurational Dirac–Fock all-electron (AE) calculations. For a thorough introduction to RECPs, see e.g. the review by Dolg and Cao [7]. The use of RECPs allows us to conveniently and accurately introduce the relativistic corrections mentioned above into a two-component Schrödinger equation, instead of having to resort to the four-component Dirac equation [8], which is more demanding computationally, and not easily amenable for a grid formulation [9–11]. In quantum chemistry applications, methods employing RECPs are considered *ab initio*, as they can be systematically improved [12–14]. It should be noted that RECPs treat some of the relativistic terms, most notably the electron–electron spin–orbit interaction, only in the mean-field sense. Nonetheless, the errors introduced by this approximation are generally small compared to the errors introduced by the CIS *Ansatz* [15, 16]. In contrast, previous work considering spin–orbit interaction on the TD-CIS level [4, 17] consists of rotating from the $n\ell m_\ell s m_s$ basis

to the $n\ell j m_j$ basis and by introducing the experimental ionization potentials for the $J = 1/2$ and $J = 3/2$ (where J is the total angular momentum of the residual ion) channels, respectively.

II.3. TIME PROPAGATOR

The higher symmetry of the atomic case can be utilized when designing the propagator, which is more efficient, but somewhat involved. The chief reason for not using a polynomial approximation to the matrix exponential, such as 4th order Runge–Kutta (RK4) or Krylov iterations, is the spectral range of the Hamiltonian which in spherical coordinates is dominated by the centrifugal potential

$$V_\ell(r) = \frac{\ell(\ell+1)}{2r^2}, \quad (\text{II-2})$$

the highest eigenvalue of which is on the order of $\ell_{\text{max}}^2/r_{\text{min}}^2$. This severely limits the largest time step that can be taken by the propagator. Instead, we opt for a second-order palindromic Strang splitting [18] (cf. the symmetric Baker–Campbell–Hausdorff formula) of the propagator

$$\exp\left[\mathcal{T} \int_0^\tau dt M(t)\right] = \dots e^{\tau C/2} e^{\tau B/2} e^{\tau A} e^{\tau B/2} e^{\tau C/2} \dots + \mathcal{O}\{\tau^3([A, B] + [A, C] + [B, C] + \dots)\},$$

where $\frac{1}{\tau} \int_0^\tau dt M(t) = A + B + C\dots$ is the matrix representation of the Hamiltonian $-i\hat{H}(t)$ integrated over the time step τ , and \mathcal{T} is the time-ordering operator. This splitting lets us tailor a propagator for each part of the Hamiltonian which may have vastly different spectral and spatial properties, e.g. the centrifugal potential (II-2) can trivially be exponentiated exactly, circumventing the issues of large spectral radius which is problematic for polynomial approximations. In contrast, a simple RK4 propagator is used for the Coulomb interaction, whose spectral radius is rather limited, but which is costly to evaluate. The use of RK4 makes the propagator only conditionally stable, however this has not been found to be a problem in practice. Finally, since the overall split-

ting is second-order in time, it is enough to integrate the time-dependent terms of the Hamiltonian to the same order, for instance via evaluation at the centre of the time step.

Which terms appear in the splitting depends on the particular system, but the general structure is

$$\mathcal{U} = \mathfrak{a}^{\tau D/2} e^{\tau A} e^{\tau D/2} + \mathcal{O}\{\tau^3[\dots]\},$$

where A contains the field-free Hamiltonian, D the dipole interaction, and \mathfrak{a} indicates that any possible subsplitting is applied in reverse (to preserve unitarity to $\mathcal{O}\{\tau^3\}$). In the most complicated case, with dipole couplings between the occupied orbitals (e.g. in neon), and spin–orbit interaction, the full propagator reads

$$\mathcal{U} = \mathfrak{a}^{\tau D_{kl}/2} \mathfrak{a}^{\tau D_{\bar{k}}/2} \mathfrak{a}^{\tau D_{k\bar{k}}/2} \mathfrak{a}^{\tau A_{1b}/2} \mathfrak{a}^{\tau A_{s-o}/2} e^{\tau A_{2b}} e^{\tau A_{s-o}/2} e^{\tau A_{1b}/2} e^{\tau D_{\bar{k}\bar{k}}/2} e^{\tau D_{\bar{k}}/2} e^{\tau D_{kl}/2} + \mathcal{O}\{\tau^3[\dots]\}, \quad (\text{II-3})$$

whereas in the non-relativistic single-active electron

(SAE) case (e.g. hydrogen), the propagator reduces to

$$\mathcal{U} = \mathfrak{a}^{\tau D_{\bar{k}}/2} e^{\tau A_{1b}} e^{\tau D_{\bar{k}}/2} + \mathcal{O}\{\tau^3[A_{1b}, D_{\bar{k}}]\}.$$

The various subterms will be enumerated and described in the following sub-sections.

We note that the above scheme is similar in spirit to those of Sato *et al.* [19] and Teramura *et al.* [20], but differs in details. The latter has higher convergence order than the present work, but relies on the φ_k matrix functions [21] which can be numerically delicate to implement. Additionally, our scheme is rather different from earlier atomic TD-CIS implementations described in the literature: Rohringer *et al.* [3] used RK4 since they only considered 1D systems where the centrifugal potential does not appear; Rohringer and Santra [4] and Greenman *et al.* [5] instead represent their wavefunctions in the basis of the singly excited Slater determinants (which yields block-dense dipole and Coulomb matrices), using a second-order differencing propagator. Compared to these implementations, our scheme can handle comparatively large time steps.

A. Propagation on a submanifold

When propagating the EOMs (I-5[†]), we are solving a partial differential equation on a submanifold $\mathcal{M} \subset \mathcal{H}$, due to the constraint that the particle orbitals must at all times remain orthogonal to the occupied orbitals; in general, $\hat{H}\Psi \notin \mathcal{M}$. This means that instead of computing the matrix exponential $U = \exp(A)$, as we would ordinarily do if the solution was allowed to occupy any part of the Hilbert space \mathcal{H} , we need to compute its projected counterpart

$$U_p = \exp(\hat{P}A\hat{P}), \quad \hat{P} = \hat{\mathbf{1}} - \hat{Q}, \quad \hat{Q} = |i\rangle\langle i|.$$

Normally, for a matrix A with a similarity transform S, we have

$$\exp(SAS^{-1}) = S \exp(A) S^{-1},$$

which is most easily proved using the k th term of the Taylor expansion of the exponential function:

$$\frac{(SAS^{-1})^k}{k!} = S \frac{A^k}{k!} S^{-1}.$$

We cannot use this relation in the present case since the projectors are idempotent:

$$\hat{P}^2 = \hat{P} \implies \exp(\hat{P}A\hat{P}) \neq \hat{P} \exp(A) \hat{P},$$

and making this approximation would reduce convergence of the time propagator to first order.

Furthermore, since \hat{P} is spatially dense, any sparsity pattern of A that we hoped to benefit from seems lost. However, we can use the fact that the occupied orbitals $|i\rangle$ from which the projectors are constructed are spatially confined to the extents of the HF reference, together with the splitting:

$$\hat{P}A\hat{P} = (\hat{\mathbf{1}} - \hat{Q})A(\hat{\mathbf{1}} - \hat{Q}) = A + \underbrace{(-\hat{Q}A - A\hat{Q} + \hat{Q}A\hat{Q})}_{\stackrel{\text{def}}{=} A_{\hat{Q}}}. \quad (\text{II-4})$$

Since \hat{Q} is the projector onto the space of occupied orbitals, it is limited in extent, i.e. it has compact support, which in turn means that $A_{\hat{Q}}$ has compact support. This is crucial, because it means we can precompute the exponential of $A_{\hat{Q}}$ via exact diagonalization, and we can approximate $\exp(\tau A)$ using any method of our choosing.

Finally, $\hat{P}\Psi$ projects Ψ onto the submanifold \mathcal{M} , and conversely $\hat{Q}\Psi$ is then the *rejection*. We thus term $A_{\hat{Q}}$ the *rejector* of A. To illustrate the efficacy of the rejector splitting (II-4), we consider the dipole interaction (see II.3D below); in Figure 1, the sparsity patterns of the dipole interaction D, and its projectors and rejectors are shown. Since in finite-differences, potentials are represented by diagonal matrices, non-zero blocks of D only have entries on their diagonals. The other matrices are, as labelled, the sparsity patterns of the projection \hat{Q} onto the occupied orbitals, which is non-zero only for those to particle orbitals that are in the same symmetries as the two occupied orbitals of the HF reference; the rejector $D_{\hat{Q}} = -\hat{Q}D - D\hat{Q} + \hat{Q}D\hat{Q}$, which is spatially compact since it 1) only couples a few particle orbitals, and 2) radially only encompasses the extents of the HF reference, thereby not filling the whole matrix block; and the projected dipole $\hat{P}D\hat{P}$, which is the operator we wish to approximate the exponential of, but whose sparsity pattern is unfavourable to any approximations beyond polynomial methods. In this illustrative example, the HF problem is solved on the radial interval 0 Bohr to 7 Bohr, whereas the dipole is computed on the interval 0 Bohr to 10 Bohr; in a more realistic scenario, the dipole operator is required for $r \gg 10$ Bohr, increasing the numerical utility of this operator splitting.

When approximating $\exp(-i\tau\hat{P}D\hat{P})$ by $\exp(-i\tau D_{\hat{Q}}/2)\exp(-i\tau D)\exp(-i\tau D_{\hat{Q}}/2)$, and varying the time step τ , the local error is cubic in τ , which leads to a second-order propagator overall (see Figure 2).

B. One-body atomic Hamiltonian

The one-body part of the atomic Hamiltonian, labelled A_{1b} in (II-3), contains the kinetic energy and one-body potential energy of the electron:

$$\hat{h} \stackrel{\text{def}}{=} \frac{p^2}{2} + \frac{\ell(\ell+1)}{2r^2} + V_C(r) + V_{\text{CAP}}(r), \quad (\text{II-5})$$

where the *complex absorbing potential* (CAP) $V_{\text{CAP}}(r)$ is usually taken to be that of Manolopoulos [22]. Since in finite-differences, the matrix representation of (II-5) is a tridiagonal matrix, we use the Crank–Nicolson method to approximate the matrix exponential. The orbitally diagonal part of the direct interaction \hat{J}_{ii} (see next section), i.e. the Hartree potential, is although formally a two-body operator, effectively a one-body potential and as such a diagonal matrix, which we exponentiate together with \hat{h} .

Acting with \hat{h} on a particle orbital $|\tilde{k}\rangle$ can take us out of the correct submanifold, as described in the preceding

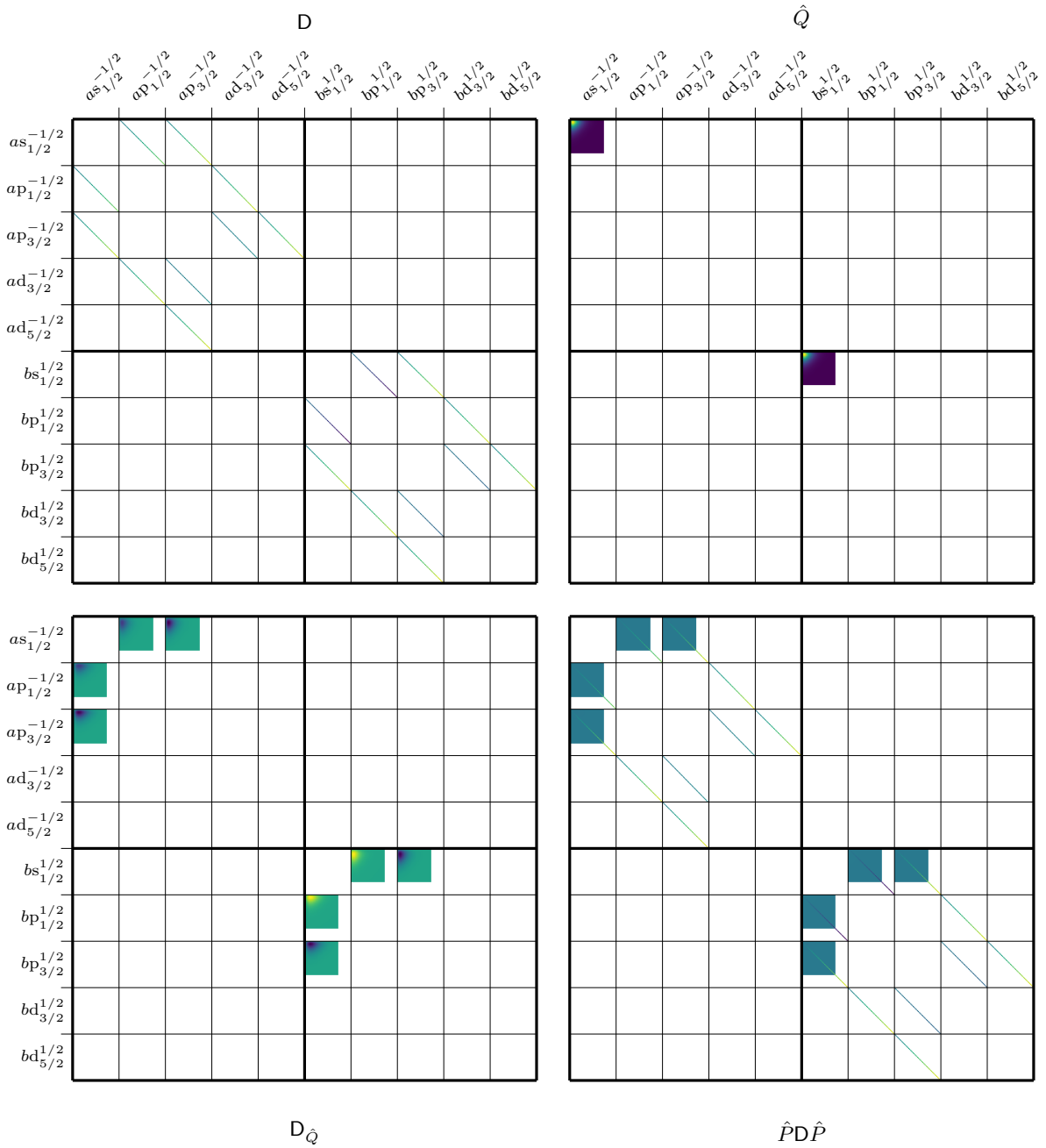


FIG. 1. Sparsity pattern of dipole operator D , in the case of helium in the $n\ell jm_j$ basis ($\ell \in \{s, p, d\}$) and linear polarization ($\implies \Delta m_j = 0$). Each block corresponds to coupling between a pair of particle orbitals, which are labelled by their particles $\ell_j^{m_j}$, and their holes $a \iff 1s_{1/2}^{-1/2-1}$ and $b \iff 1s_{1/2}^{1/2-1}$. See main text for discussion.

section. We therefore precompute $\exp(-i\tau\hat{h}_{\hat{Q}}/2)$, where $\hat{h}_{\hat{Q}}$ is defined in (II-4), and place this on either side of the Crank–Nicolson propagator for \hat{h} .

Even though adding a CAP may be seen as a pragmatic approach to avoid unwanted reflections, they are systematically improvable to the point that they are formally equivalent to exterior complex scaling [23–29]. TD-CIS with the addition of a CAP can thus still be considered *ab initio* [5].

C. Coulomb interaction

The Coulomb interaction, labelled A_{2b} in (II-3), enters the TD-CIS EOMs (I-5†) through the Fock operator $\hat{f} = \hat{h} + \hat{J}_{ii} - \hat{K}_{ii}$ which appears on the orbital diagonal, as well as the configuration interaction term $\hat{J}_{lk} - \hat{K}_{lk}$ which couples the different particle–hole channels. Since the occupied orbitals remain fixed in the TD-CIS *Ansatz*, both \hat{J} and \hat{K} remain formally time-independent. However,

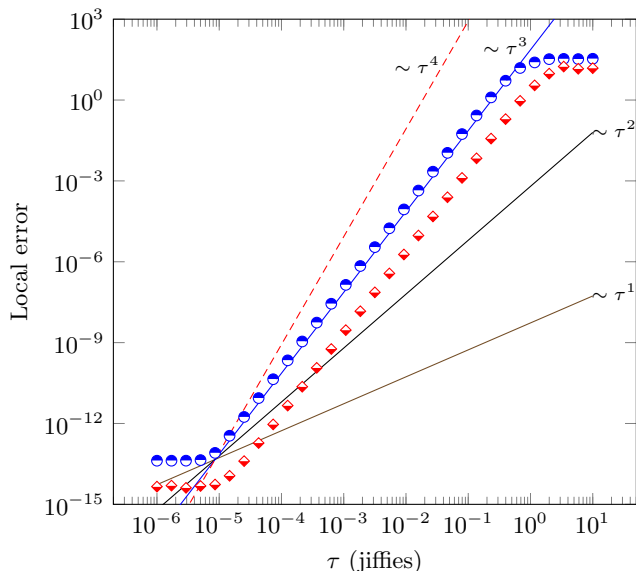


FIG. 2. Performance of the Strang splitting of the projected dipole illustrated in Figure 1; the blue circles indicate the local error $\|\exp(-i\tau\hat{P}\mathbf{D}\hat{P}) - \exp(-i\tau\mathbf{D}_{\hat{Q}}/2)\exp(-i\tau\mathbf{D})\exp(-i\tau\mathbf{D}_{\hat{Q}}/2)\|_2$ as a function of the time step τ . $\exp(-i\tau\hat{P}\mathbf{D}\hat{P})$ is computed exactly via diagonalization, $\exp(-i\tau\mathbf{D})$ via Givens rotations (see section III.3.D below), and $\exp(-i\tau\mathbf{D}_{\hat{Q}}/2)$ using RK4. The straight lines show that the local error indeed is of $\mathcal{O}\{\tau^3\}$, as expected. Another measure of the accuracy shown as red diamonds, is $\|\hat{Q}\exp(-i\tau\mathbf{D}_{\hat{Q}}/2)\exp(-i\tau\mathbf{D})\exp(-i\tau\mathbf{D}_{\hat{Q}}/2)\hat{P}\|_2$, the norm of the *rejection of the split-propagator itself*, i.e. how much the split-propagator populates $\perp \mathcal{M}$, i.e. the orthogonal complement of the submanifold. This measure also behaves as $\mathcal{O}\{\tau^3\}$.

whereas \hat{J} is only non-local in the spin–angular coordinates (and thus radially diagonal), \hat{K} is also radially non-local, preventing its storage as a structured matrix. On the other hand, \hat{K} has radially compact support. To see this, we rewrite the Coulomb interaction (I-1) in spherical coordinates [see Equation (5.17.9) of 2]:

$$[ab|cd] = \sum_k C_{abcd}^k \int_0^\infty dr_1 P_a^*(r_1) \frac{Y_{bd}^k(r_1)}{r_1} P_c(r_1),$$

where C_{abcd}^k are Clebsch–Gordan coefficients, and the k th multipole of the repulsion potential formed by the orbitals χ_i, χ_j is given by

$$\begin{aligned} Y_{ij}^k(r_1) &\stackrel{\text{def}}{=} r_1 \int_0^\infty dr_2 \frac{r_2^k}{r_1^{k+1}} P_i^*(r_2) P_j(r_2) \\ &= \int_0^{r_1} dr_2 \left(\frac{r_2}{r_1}\right)^k P_i^*(r_2) P_j(r_2) \\ &\quad + \int_{r_1}^\infty dr_2 \left(\frac{r_1}{r_2}\right)^{k+1} P_i^*(r_2) P_j(r_2), \end{aligned}$$

and $P_i(r), P_j(r)$ are the radial components of the orbitals. These potentials are found by solving Poisson’s prob-

lem [30–33], with the mutual charge density $\rho_{ij}(r) = P_i^*(r)P_j(r)$ as the inhomogeneous source term. In the TD-CIS *Ansatz*, this charge density is formed from one (in case of \hat{K}) or two (in case of \hat{J}) occupied orbitals, which means we only have to solve Poisson’s problem on the radial extent of the HF reference. However, we then need to add in a homogeneous contribution as well, that accounts for the long-range behaviour; this is only trivial to do in the spherically symmetric case and is an important optimization over the general case, where instead Poisson’s problem has to be solved over the entire domain (however, in that case an asymptotic multipole solution may be used as the initial guess, speeding up convergence of the solution).

From this argument, we see that $Y_{ij}^k(r)$ for the direct interaction \hat{J} will be formed from two occupied orbitals $|i\rangle, |j\rangle$, and will thus be time-independent and radially diagonal (i.e. represented by a diagonal matrix in finite-differences), however, it will extend over the whole computational domain. In contrast, to compute the exchange interaction \hat{K} , the mutual charge density is formed from an occupied orbital $|i\rangle$ and the time-dependent particle orbital $|\tilde{l}\rangle$ which \hat{K} acts on, which means the resulting potential is radially non-local. The mutual charge density will have zero trace, and $Y_{i\tilde{l}}^k(r)$ for \hat{K} will decay as at least r^{-2} . Additionally, it is subsequently applied to an occupied orbital, which decays as $\exp(-\sqrt{2}|\epsilon_i|r)$. Thus the \hat{K} operator is radially localized to the HF reference. Acting with \hat{J} on the wavefunction thus amounts to multiplying with precomputed radially diagonal matrices, and acting with \hat{K} amounts to solving a radially localized Poisson problem. These operations are the limiting factors of the time propagator.

Since the Coulomb interaction is of limited spectral range, a polynomial approximation to the matrix exponential that has a fixed number of matrix–vector products per step (such as RK4), is entirely satisfactory. Maintaining orthogonality of the particle orbitals with respect to the occupied orbitals is trivial by projecting out the latter after each RK4 stage. This procedure is similar to the approach taken by Sato *et al.* [19].

D. Dipole interaction

The interaction with the external laser field is treated in the dipole approximation, where the two most common choices for the interaction operator are

$$\hat{V}_L(t) = \begin{cases} \mathbf{F}(t) \cdot \mathbf{r}, & \text{(length gauge),} \\ \mathbf{A}(t) \cdot \mathbf{p} + \frac{A^2(t)}{2}, & \text{(velocity gauge).} \end{cases}$$

Although the TD-CIS *Ansatz* with frozen core orbitals is gauge variant [34–36], we have implemented dipole interaction for both gauges; all results presented in the present work are however computed in the length gauge.

There are three terms we need to consider, the *source–virtual* dipole interaction $\langle k|\hat{V}_L|\tilde{k}\rangle$, the *virtual–virtual*

dipole interaction $\langle \tilde{k} | \hat{V}_L | \tilde{k} \rangle$, and the *source–source* dipole interaction $\langle k | \hat{V}_L | l \rangle$ (may be absent in some systems).

1. Source–virtual dipole interaction

This interaction, labelled $D_{k\tilde{k}}$ in (II-3), corresponds to the sub-EOMs

$$\begin{aligned} i\partial_t c_0 &= \langle k | \hat{V}_L | \tilde{k} \rangle, \\ i\partial_t |\tilde{k}\rangle &= c_0 \hat{V}_L |k\rangle - \lambda_{\tilde{k}i} |i\rangle, \end{aligned} \quad (\text{II-6})$$

which we call the source–virtual dipole interaction, since the occupied orbital $|k\rangle$ constitutes a source term for the particle orbital $|\tilde{k}\rangle$, which in turn is a linear combination of virtual orbitals. We can rewrite the EOMs (II-6) in matrix form

$$i\partial_t q = \underbrace{\begin{bmatrix} 0 & \langle m | \\ |m\rangle & 0 \end{bmatrix}}_{\stackrel{\text{def}}{=} A} q, \quad q \stackrel{\text{def}}{=} \begin{bmatrix} c_0 \\ |\tilde{m}\rangle \end{bmatrix}, \quad (\text{II-6}^*)$$

where the matrix A is non-zero only in the first column and row, respectively, and

$$|m\rangle \stackrel{\text{def}}{=} \begin{bmatrix} \hat{P}\hat{V}_L |k\rangle \\ \hat{P}\hat{V}_L |l\rangle \\ \vdots \end{bmatrix}, \quad |\tilde{m}\rangle \stackrel{\text{def}}{=} \begin{bmatrix} |\tilde{k}\rangle \\ |\tilde{l}\rangle \\ \vdots \end{bmatrix}.$$

The projector \hat{P} in $|m\rangle$ ensures orthogonality of the particle orbitals to the occupied orbitals, after applying the source–virtual dipole interaction. Since the laser interaction $\hat{V}_L = \mathbf{F}(t) \cdot \mathbf{r}$ is time-dependent, $|m\rangle$ has to be recomputed every time step. However, the projected polarized source orbitals

$$\begin{bmatrix} \hat{P}\hat{d} |k\rangle \\ \hat{P}\hat{d} |l\rangle \\ \vdots \end{bmatrix}, \quad \hat{d} = \hat{x}, \hat{y}, \hat{z},$$

can be precomputed, and linearly combined with the time-dependent field components $F_d(t)$.

Having formed the matrix EOMs (II-6^{*}), we can solve it exactly, if we can form the singular-value decomposition (SVD) of $A = \tilde{A}S\tilde{A}^\dagger$ (this choice is possible if A is Hermitian):

$$\exp(\mu A)q = \{S[\exp(\mu\tilde{A}) - \hat{\mathbf{1}}]S^\dagger + \hat{\mathbf{1}}\}q. \quad (\text{II-7})$$

For the A we have in TD-CIS, the SVD that decomposes A is given by

$$\begin{aligned} \tilde{A} &\stackrel{\text{def}}{=} \begin{bmatrix} s & 0 \\ 0 & -s \end{bmatrix}, \quad s \stackrel{\text{def}}{=} |\langle m | m \rangle| \\ \implies \exp(\mu\tilde{A}) - \hat{\mathbf{1}} &\equiv \begin{bmatrix} e^{\mu s} - 1 & 0 \\ 0 & e^{-\mu s} - 1 \end{bmatrix}, \end{aligned}$$

and the left-singular vectors are given by

$$S \stackrel{\text{def}}{=} \frac{1}{\sqrt{2}s} \begin{bmatrix} s & -s \\ |m\rangle & |m\rangle \end{bmatrix}.$$

One time step with the source–virtual dipole interaction can thus be accomplished by

$$\begin{aligned} \begin{bmatrix} c_0 \\ |\tilde{m}\rangle \end{bmatrix} &\leftarrow \begin{bmatrix} c_0 \\ |\tilde{m}\rangle \end{bmatrix} \\ &+ \frac{1}{2s^2} \begin{bmatrix} s & -s \\ |m\rangle & |m\rangle \end{bmatrix} \begin{bmatrix} e^{\mu s} - 1 & 0 \\ 0 & e^{-\mu s} - 1 \end{bmatrix} \begin{bmatrix} c_0 s + \langle m | \tilde{m} \rangle \\ -c_0 s + \langle m | \tilde{m} \rangle \end{bmatrix}. \end{aligned} \quad (\text{II-7}^*)$$

The advantage of this formulation, is that the complexity of the matrix exponential reduces to linear in the size of the compact HF support. We note that although our EOMs (I-5[†]) are non-Hermitian due to the presence of a CAP, we still have that $|m\rangle^\dagger \equiv \langle m|$, since $|m\rangle$ is formed as a linear combination of projected polarized source orbitals, and thus of the same radial extent as the HF reference, where the CAP is identically zero.

2. Virtual–virtual dipole interaction

This interaction, labelled $D_{\tilde{k}}$ in (II-3), is almost the same as in the SAE case, and therefore it is implemented analogously (see appendix B and e.g. Muller [37], Schafer [38], and Patchkovskii and Muller [39]), with added complication in those partial waves which share spin–angular quantum numbers with the occupied orbitals of the HF reference; for those we employ the ideas detailed in section II.3.A. Specifically, for the propagation of the rejecor of the dipole, $D_{\hat{Q}}$, we use RK4 to approximate the matrix exponential.

For systems treated in the $nljm_j$ basis, we temporarily change to the $nlm_\ell sm_s$ basis via a unitary transformation (built from Clebsch–Gordan coefficients), since the dipole interaction is sparser in that representation.

3. Source–source dipole interaction & spin–orbit interaction

For systems where there are dipole moments between the occupied orbitals (e.g. neon), the dipole interaction can trigger transitions between the channels; we call this source–source dipole interaction, and it is labelled D_{kl} in (II-3). For each pair $|k\rangle, |l\rangle$ of orbitals which have a non-zero dipole moment, the corresponding pair of particle orbitals $|\tilde{k}\rangle, |\tilde{l}\rangle$ are mixed using a Givens rotation (cf. appendix B) where the rotation angle is $a = \mathbf{F}(t) \cdot \mathbf{d}_{kl}$, and the dipole moment $\mathbf{d}_{kl} \stackrel{\text{def}}{=} \langle \chi_k | \mathbf{r} | \chi_l \rangle$ is precomputed. Exactly the same approach is taken in the case of spin–orbit interaction between occupied orbitals [labelled A_{s-o} in (II-3), e.g. 4p and 5p in xenon], with the only difference that the spin–orbit interaction is time-independent.

4. General polarization

The Cartesian operators x, y, z commute, however in a truncated spherical basis only approximately so, e.g. the commutator $[z, x]$ is non-zero only in the highest considered ℓ channel. We can thus safely use the splitting $\exp(\mu\mathbf{F} \cdot \mathbf{r}) = \exp(\mu F_x x) \exp(\mu F_y y) \exp(\mu F_z z)$, as long as the population in the highest ℓ channel is negligible. We stay in the lab frame, i.e. we do not rotate the wavefunction as done by Muller [37] and Patchkovskii and Muller [39], since although that would potentially be more efficient, it would require the rotation of the occupied orbitals $|i\rangle, |j\rangle$ (and hence the potentials \hat{J}_{ij} and \hat{K}_{ij}), in addition to the particle orbitals $|\tilde{i}\rangle, |\tilde{j}\rangle$ (which are the analogues of the wavefunctions in the SAE case). Although this is technically possible, the numerical implementation is non-trivial and error-prone.

II.4. EXAMPLE CALCULATIONS

Unless otherwise specified, the calculations below use *truncated* Gaussian pulse envelopes [39] for the vector potential:

$$\mathbf{A}(t) = \mathbf{A}_0 \exp[-\alpha f(t)] \sin(\omega t + \phi),$$

$$f(t) \stackrel{\text{def}}{=} \begin{cases} |t|^2, & |t| \leq t_{\text{off}}, \\ \left| t_{\text{off}} + \frac{2t_{\text{mo}}}{\pi} \tan\left(\frac{\pi}{2} \frac{|t| - t_{\text{off}}}{t_{\text{mo}}}\right) \right|^2, & t_{\text{off}} < |t| \leq t_{\text{max}}, \\ +\infty, & \text{else,} \end{cases} \quad (\text{II-8})$$

where the helper function $f(t)$ ensures a smooth turn-off of the field starting at t_{off} and finishing at t_{max} ($t_{\text{mo}} \stackrel{\text{def}}{=} t_{\text{max}} - t_{\text{off}}$). The parameter α is determined such that the full-width half-maximum T of the intensity envelope is the desired pulse duration; since $\mathbf{F}(t) \stackrel{\text{def}}{=} -\partial_t \mathbf{A}(t)$ the map from T to α is in general dependent on the carrier angular frequency ω , but in the long-pulse limit $\alpha \rightarrow 2 \ln 2 / T^2$. Typically, we choose $t_{\text{off}} = 4\sigma$ and $t_{\text{max}} = 6\sigma$, where the standard deviation of the intensity envelope is given by $\sigma = T / (2\sqrt{2 \ln 2})$. The main benefit of this pulse shape is the suppression of side-lobes in the spectrum (which can lead to e.g. overestimation of one-photon cross-sections), while still maintaining a minimal time-bandwidth product. An example spectrum for a two-colour field with the envelope (II-8) is shown in Figure 6 (b).

For the example calculations presented below, the radial grid employed is smoothly approaching a uniform grid according to the formula [40]:

$$r_j = r_{j-1} + \rho_{\text{min}} + (1 - e^{-\alpha r_{j-1}})(\rho_{\text{max}} - \rho_{\text{min}}), \quad (\text{II-9})$$

with the first grid point at $r_1 = \rho_{\text{min}}/2$. This yields an approximately log–lin behaviour with a dense grid close to the origin where the bound orbitals exhibit a very oscillatory behaviour. The asymptotic grid spacing should be chosen to fulfil the Nyquist sampling theorem

for the highest momentum desired: $\rho_{\text{max}} \lesssim (2k_{\text{max}})^{-1} = (8W_{k_{\text{max}}})^{-1/2}$, where $W_{k_{\text{max}}} = 4 \text{ Ha}$, unless otherwise specified. The specific grid parameters are given in Table I.

TABLE I. Radial grid parameters used for the example calculations.

	H	He	Ne AE	Ne RECP	Xe RECP
$\rho_{\text{min}}(\text{Bohr})$	0.3	0.15	0.1	0.125	3/26
α	0.1	0.1	0.1	0.3	0.3

The number of partial waves scales quadratically with the maximum orbital angular momentum ℓ_{max} , and linearly with number of channels n_c :

$$n_p = 2(\ell_{\text{max}} + 1)^2 n_c, \quad (\text{II-10})$$

where the factor of 2 comes from the spin of the excited electron. In the case of linear polarization along z , where $\Delta m_\ell = 0$ ($\Delta m_j = 0$), this reduces to

$$n_p < \kappa(\ell_{\text{max}} + 1)n_c, \quad \kappa = \begin{cases} 1, & n\ell m_\ell s m_s, \\ 2, & n\ell j m_j, \end{cases} \quad (\text{II-11})$$

where we can only give an upper bound since ℓ_{min} depends on the ionization channel (i.e. $\ell \geq |m_\ell|$).

A. Static polarizability

The static polarizability is equivalent to the Stark shift, i.e. how much the ground state moves when applying a static electric field of amplitude F :

$$E(I) = E_0 - \frac{\alpha(0)}{2} F^2 - \frac{\beta(0)}{4} F^4 - \frac{\gamma(0)}{6} F^6 - \frac{\delta(0)}{8} F^8 - \dots$$

For hydrogen, the first few values are [43]

$$\alpha(0) = \frac{9}{2}, \quad \beta(0) = \frac{3555}{16},$$

$$\gamma(0) = \frac{2\,512\,779 \times 6}{512}, \quad \delta(0) = \frac{13\,012\,777\,803}{2048}.$$

We compute the static polarizability in a dynamic fashion [see section 6.1 of 44] by applying a static field over a length of time (i.e. sudden approximation), starting from an initial state Ψ_i that is a linear combination of a few low-lying states

$$|\Psi_i\rangle = c_n |n\rangle.$$

At each time step, we compute the overlap of the wavefunction with the initial state:

$$C(t) = \langle \Psi_i | \Psi(t) \rangle = \langle \Psi_i | \mathcal{T} \exp \left[-i \int_0^t d\tau \hat{H}(\tau) \right] | \Psi_i \rangle$$

$$= e^{-iE_m t} |\langle m | \Psi_i \rangle|^2,$$

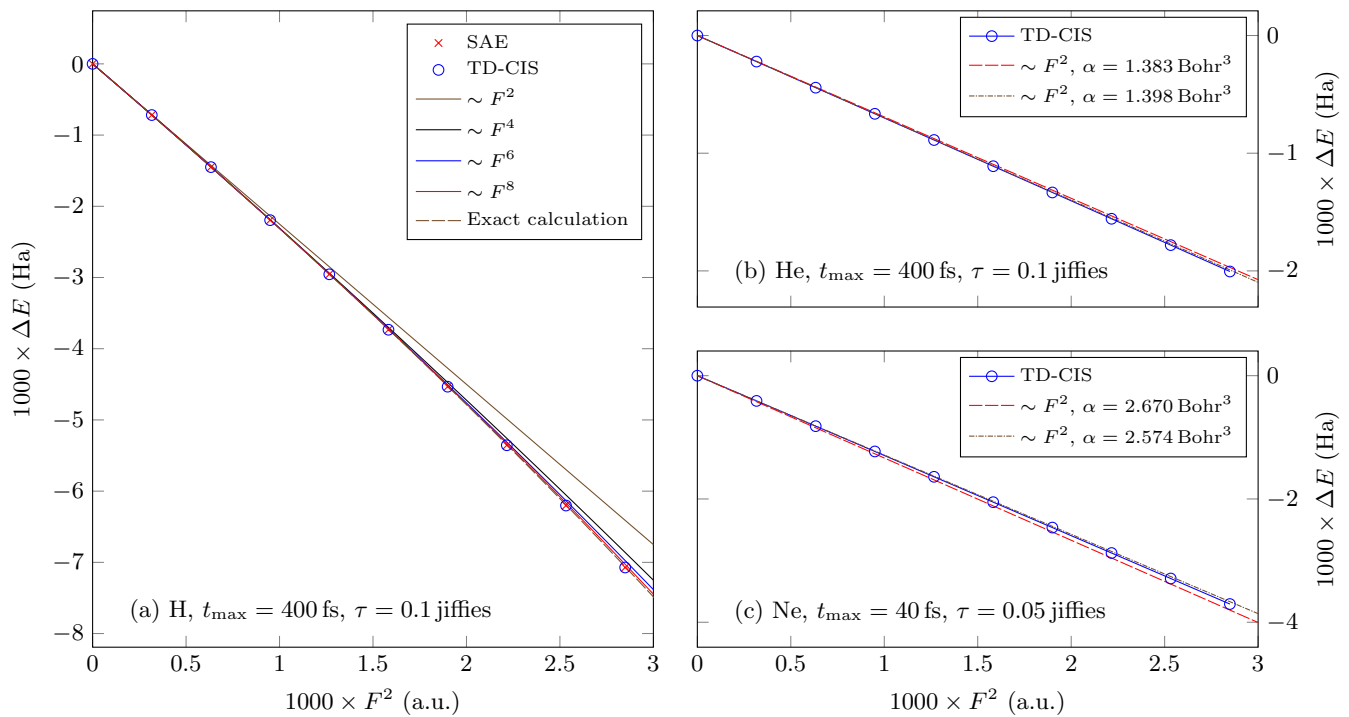


FIG. 3. Static polarizability of (a) hydrogen, (b) helium, and (c) neon, as a function of static field strength F . Also plotted are expansions in powers of F^2 with coefficients taken from theory (hydrogen) or experiment (helium and neon). For hydrogen, adding more terms to the expansion in F^2 approaches the results as computed by SAE and TD-CIS. Also shown are exact calculations using the method of Kolosov [41], with which the SAE & TD-CIS results agree excellently. For helium and neon, we compare with experimental results (dashed, red) [42] and perturbation theory results (dot-dashed, grey). The static polarizability of neon as predicted by TD-CIS is slightly smaller (in magnitude) than the experimental result; the deviation can be explained by lack of correlation at the CIS level.

where in the last step we have used the fact that the field is static, the Hamiltonian is time-independent, and hence we can trivially rewrite the propagator on spectral form using the eigenstates $|m\rangle$ of the full Hamiltonian. From this we see that, as long as $\langle m|\Psi_i\rangle \neq 0$, the correlation trace $C(t)$ will contain Fourier components at $-E_m$; for moderate field strengths, the field-free ground state is a large component of the ground state of the full Hamiltonian, and we choose simply $|\Psi_i\rangle = |\Psi_0\rangle$. By repeating the calculation for different field strengths F , we can thus map $\Delta E_m(F)$, which is shown for hydrogen, helium, and neon in Figure 3.

B. Dynamic polarizability

The polarizability of a system relates the induced polarization to the moments of the electric field:

$$P^k(\omega_0; t) = \alpha(\omega_0)F^k(t) + \beta_{ij}^k(\omega_0)F^i(t)F^j(t) + \dots$$

where ω_0 is the fundamental frequency of the electric field $\mathbf{F}(t)$, α is the (dynamic) polarizability, and β is the hyperpolarizability tensor.

To first order, we can compute α by driving the system with a linearly polarized, nearly monochromatic pulse,

and dividing the Fourier transform of the induced dipole moment $z(t)$ at the driving frequency by the amplitude of the driving field:

$$\alpha(\omega_0) = \frac{\hat{Z}(\omega_0)}{\hat{F}(\omega_0)}.$$

We instead use the more numerically stable Mukamel expression [cf. e.g. Equation (4.85) of 47, for the closely related medium absorption]

$$\langle \alpha \rangle(\omega_0) \stackrel{\text{def}}{=} \frac{\int d\omega' \hat{F}_{\omega_0}^*(\omega') \hat{Z}_{\omega_0}(\omega')}{\int d\omega' \hat{F}_{\omega_0}^*(\omega') \hat{F}_{\omega_0}(\omega')},$$

which can be thought of as a weighted average, since the Fourier transform of the driving field $\hat{F}_{\omega_0}(\omega')$ is peaked around $\omega' = \omega_0$. For $\omega_0 \rightarrow 0$, the dynamic polarizabilities approach the static ones discussed in the preceding section.

In Figure 4, dynamic polarizabilities for the ground state of hydrogen, the triplet ground state of helium, and the ground state of neon are presented. In the vicinity of excited states accessible via one-photon absorption from the initial state, the polarizabilities exhibit large resonances. For comparison, we compute the dynamic polarizability of state i for the case of continuous wave (CW),

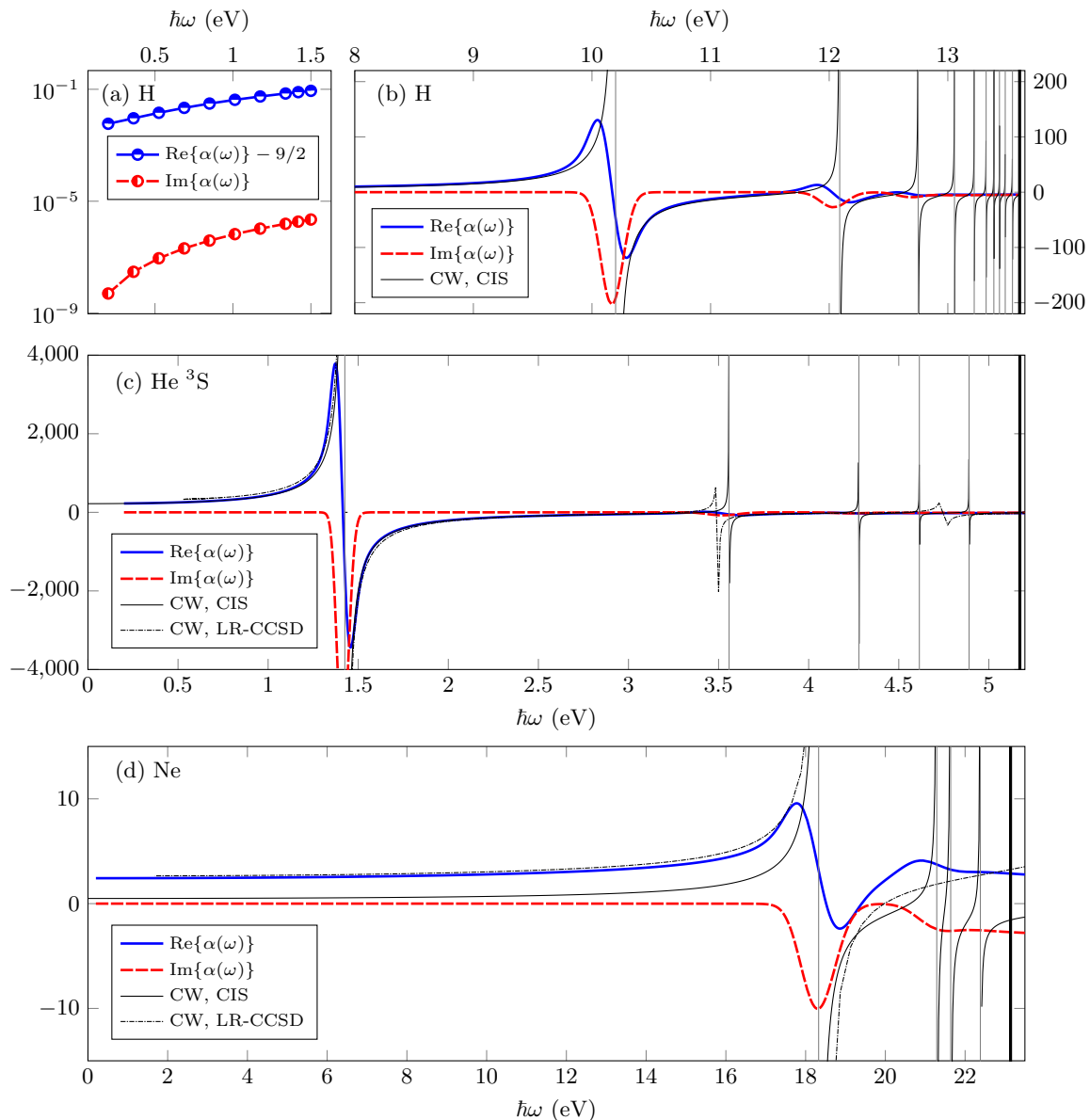


FIG. 4. (a) Dynamic polarizability of the hydrogen ground state close to the adiabatic static-field limit; number of cycles $N_c = 2$, $\ell_{\max} = d$. (b) Dynamic polarizability of the hydrogen ground state in the vicinity of the lowest resonances; $N_c = 10$, $\ell_{\max} = f$. (c) Dynamic polarization of the $1s2s^3S$ excited state of helium. The vertical lines indicate the positions of the CIS excited states. The first resonance above 1 eV is the transition to $1s2p^3P_{1,2}$; $N_c = 4$, $\ell_{\max} = g$. (d) Neon ground state; $N_c = 4$, $\ell_{\max} = g$. The first resonance around 18 eV is the transition to $1s^22s^22p^5(^2P_{3/2})3s$, which experimentally is found around 16 eV [45, 46]; the discrepancy is due to lack of correlation at the CIS level.

using the following formula that involves the field-free energy differences and dipole moments for excited states:

$$\alpha_{i;z}(\omega) = 2 \sum_{k \neq i} \frac{|\langle i|z|k \rangle|^2 E_{ki}}{E_{ki}^2 - \omega^2}, \quad E_{ki} \stackrel{\text{def}}{=} E_k - E_i. \quad (\text{II-12})$$

Additionally, for He 3S and Ne 1S , we compare with linear-response coupled-cluster singles+doubles (LR-CCSD) calculations. For He LR-CCSD is essentially exact, up to the quality of the basis set employed, in this case aug-cc-pV6Z augmented with Rydberg-like Kauf-

mann basis functions with $n \leq 8$ [48]. For Ne the aug-cc-pV6Z basis set was used. Since these reference calculations include more correlation than do the CIS results, the peaks appear at slightly different energies. To enable a more direct comparison, the curves have been shifted to approximately align the first resonance; for He the shift is 0.28 eV and for Ne 0.9 eV.

For all the dynamic polarizability calculations presented in Figure 4, the truncated Gaussian (II-8) pulse was used, with a standard deviation $\sigma = 2\pi N_c \omega^{-1}$, where ω is the driving pulse energy, and N_c the number of

cycles. $t_{\text{off}} = 3\sigma$, $t_{\text{max}} = 5\sigma$, and the intensity was $I = 10^2 \text{ W/cm}^2$. The dynamic polarizabilities for finite pulses are in excellent agreement with the perturbation theory predictions (II-12).

C. Laser-induced resonant hole coupling

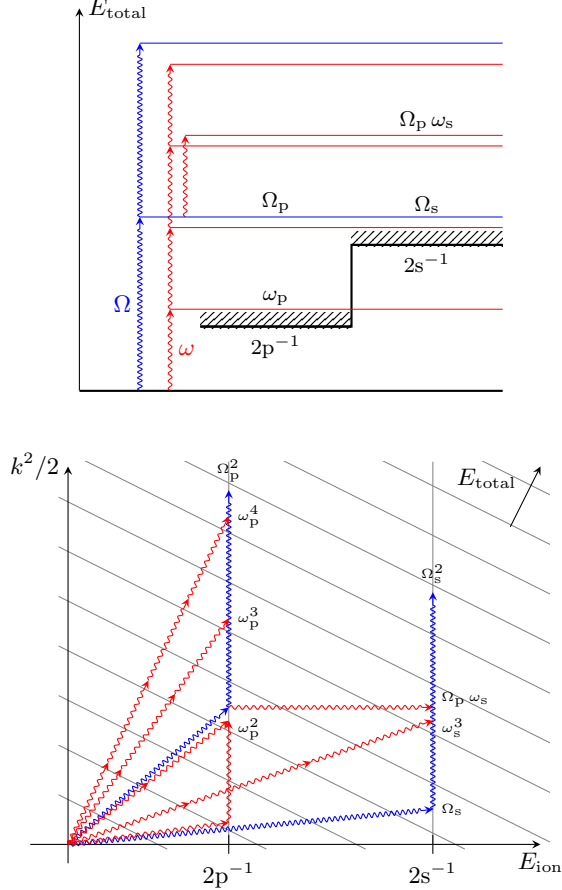


FIG. 5. Multichannel, multiphoton ionization of neon; in the CIS approximation, the $2p$ electron has an ionization potential of $\sim 23 \text{ eV}$ and the $2s$ electron $\sim 53 \text{ eV}$. The sketch illustrates weak-field ionization of neon into these two channels using a pump photon of energy Ω and a probe photon of energy ω . The horizontal thin lines indicate where we expect to find photoelectron peaks, after absorbing various combinations of Ω and ω . In the bottom panel, we show the same process in an energy-sharing diagram, where the abscissa shows energy of the ion, and the ordinate the kinetic energy of the photoelectron.

In multichannel ionization, where there is coupling between the channels, it is vital that this coupling is properly accounted for when solving the tSURFF equations of motion (I-10). An important example is the dipole coupling between the holes in the residual ion, which has the ability to move population from one channel to another, long after the photoelectron has left the vicinity of the ion. If the photoelectron wavepacket has already es-

aped the computational domain through the matching sphere at R_s , this effect must be accounted for through (I-10), otherwise there may be information missing from an ion-state resolved spectrum. An analogous problem was studied for 1D neon by You *et al.* [49].

As a simple illustration of this mechanism, we consider the ionization scheme illustrated in Figure 5, where two pulses with photon energies $\Omega > \omega$ are used. We label the photoelectron peaks according to the ionization pathways that led to them, e.g. Ω_p^2 corresponds to absorption of two photons of energy Ω , leaving the ion in state $2p^{-1}$, whereas $\Omega_p \omega_s$ corresponds to ionization into $2p^{-1}$ with one photon of energy Ω , and then channel coupling into $2s^{-1}$ via one photon of energy ω (the label ordering indicates that Ω in this case arrives before ω). In the complementary energy-sharing diagram (cf. e.g. [50]), the neutral atom is at zero energy, i.e. the origin of the coordinate system. Diagonal lines mark isolines of constant total energy of the system. Purely vertical arrows indicate absorption of a photon by the photoelectron, and similarly, purely horizontal arrows indicate absorption of a photon by the ion. Ionization requires imparting energy on both the photoelectron and the ion, which is why the corresponding arrows are diagonal. We have chosen $\omega = \Delta I_p$, which is why the photoelectron $\Omega_p \omega_s$ (diagonal, followed by horizontal arrow) will appear at the same kinetic energy as Ω_p , and close to ω_s^3 .

In Figure 6, the corresponding spectrum is shown, resolved on final ion state and kinetic energy of the photoelectron. The probe pulse with photon energy ω is delayed enough with respect to the pump pulse Ω , such that any electron ejecta due to the latter has had time to leave the computational domain entirely. The spectrum is computed both including the hole couplings as well as neglecting them, the most obvious effect of which is the disappearance of the peak $\Omega_p \omega_s$ at $\sim 40 \text{ eV}$ in the $2s^{-1}$ channel. To confirm that this peak arises mainly due to the proposed ionization pathway, i.e. $\Omega_p \omega_s$, and not the nearby possible pathways $\omega_p^2 \omega_s$ and ω_s^3 (which are both third order in terms of ω), we repeat the calculation including the hole coupling, for a range of intensities and observe the peak magnitude. Since the magnitude of this peak varies linearly with the probe pulse intensity, we conclude that it is due to absorption of one probe photon, and the pathway $\Omega_p \omega_s$ is the most likely one.

D. Spin-orbit-split Fano resonances in neon

To illustrate the power of iSURF [51] in resolving fine spectral details, we consider the ionization of neon using a broadband attosecond pulse and study the autoionization due to the Rydberg series $2s 2p^6(^2S) np^1 P_1^o$ that is embedded in the $2s^2 2p^5(^2P^o) ks, d^1 P_1^o$ continuum (see Table II for all possible pathways accessible from the ground state, through absorption of 1–3 photons). The ionization is driven by a 100 as pulse of 2 TW/cm^2 centered at $\hbar\omega = 1.124 \text{ Ha}$ (slightly above the $2p^{-1}$ threshold,

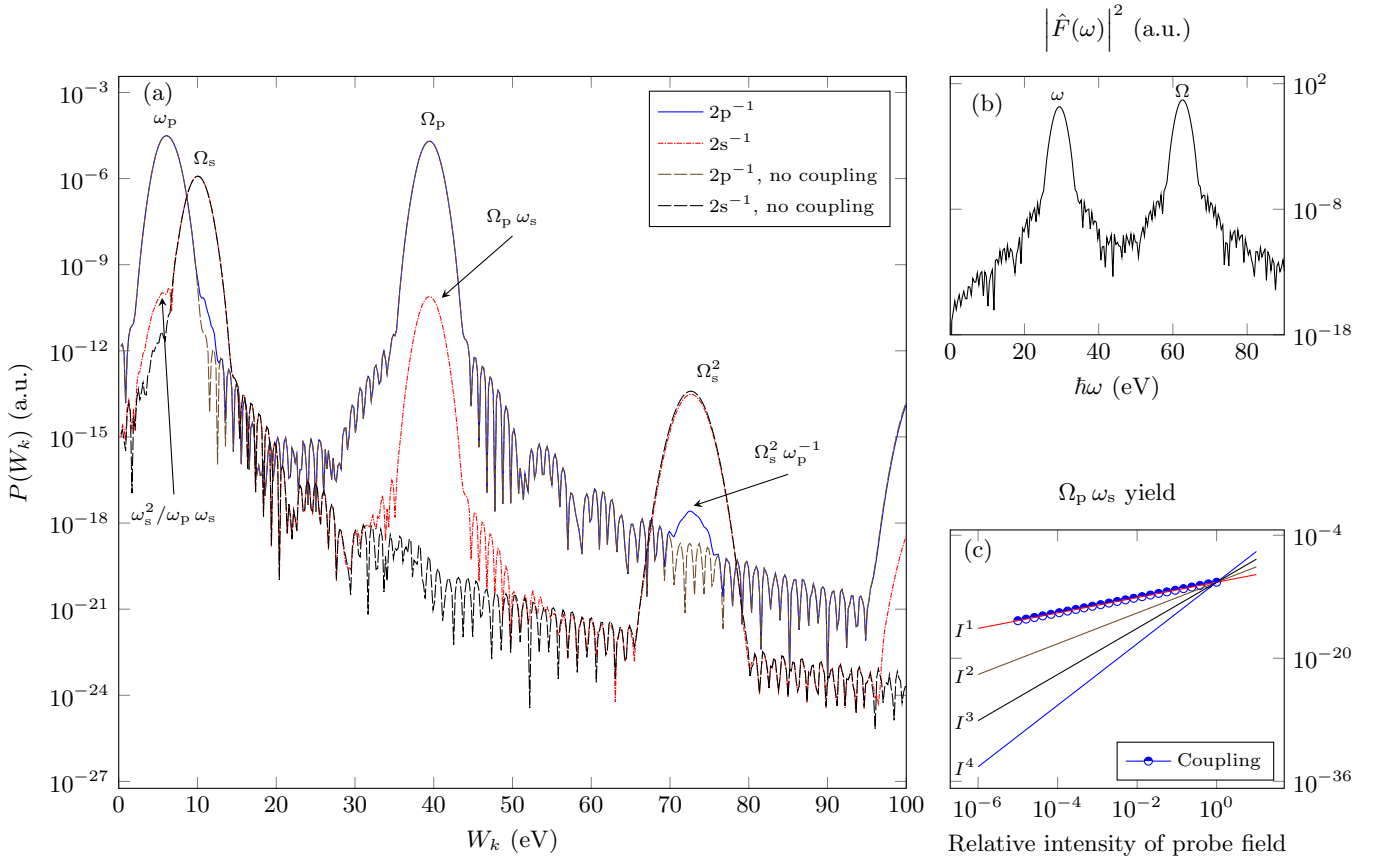


FIG. 6. Ion-resolved spectra for neon. The pump pulse has an energy of $\Omega = 2.3\text{Ha} = 62.6\text{eV}$ and an intensity of $3.51 \times 10^{10}\text{W/cm}^2$. The probe pulse has an energy matching the difference in ionization potential, i.e. $\omega \approx 29.4\text{eV}$ and an intensity of 10^{10}W/cm^2 . Both pulses have a duration of 1 fs (FWHM) and they are separated by approximately 5 fs.

but far below the $2s^{-1}$ threshold), the short pulse duration corresponds to an energy bandwidth of $\sim 11\text{eV}$. We compare spectra from AE and RECP calculations, where the RECP has been generated by Nicklass *et al.* [52].

TABLE II. Ionization channels accessible from the ground state of neon $1s^2 2s^2 2p^6\ ^1S$, through the absorption of at least q photons. The triplet terms are inaccessible in LS coupling, but spin-orbit interaction breaks this selection rule.

Channel	ℓ	q	Terms
$2s^2 2p^5\ (^2P^{\circ}_j) k\ell$	s	1	$^1P^{\circ}, ^3P^{\circ}$
	p	2	$^1S, ^1P, ^1D, ^3S, ^3P, ^3D$
	d	1	$^1P^{\circ}, ^1D^{\circ}, ^1F^{\circ}, ^3P^{\circ}, ^3D^{\circ}, ^3F^{\circ}$
	f	2	$^1D, ^1F, ^1G, ^3D, ^3F, ^3G$
$2s 2p^6\ (^2S) n\ell$	s	2	$^1S, ^3S$
	p	1	$^1P^{\circ}, ^3P^{\circ}$
	d	2	$^1D, ^3D$
	f	3	$^1F^{\circ}, ^3F^{\circ}$

Due to the spin-orbit interaction, the two allowed values of total angular momentum for the intermediate term are $J = 3/2, 1/2$, which leads to a splitting of the autoionization resonances by approximately $\Delta E_{s-o} = 0.1\text{eV}$; see

Table III. The observed discrepancy between the orbital energies of the AE calculation and the HF limit values reported by Froese Fischer [30] is mostly due to the radial grid employed (II-9), which is not dense enough close to the origin to accurately represent the $1s$ orbital. This is also reflected in the total energy. However, since the $1s$ orbital is the same in the initial and final states, this error exactly cancels. The RECP results also differ from the reference energies for the same reason; the $1s$ orbital is represented using the RECP. We note that our spin-orbit splitting ($4.92\text{mHa} \approx 0.134\text{eV}$) is slightly closer to the experimental value 0.097eV than what we are able to achieve with the aug-cc-pVQZ basis set at the CIS level. Our splitting is also close to the values computed using RCIS [8], even if the absolute orbital energies are slightly shifted.

An example photoelectron spectrum, calculated at various levels of theory, is illustrated in Figure 7. The ΔE_{s-o} splitting of the lines is clearly resolved; the corresponding quantum beat period is $T_{\text{QB}} = 2\pi/\Delta E_{s-o} \sim 43\text{fs}$. A normal photoelectron spectrum calculation using tSURFF only would necessitate post-propagation of the wavefunction, after the ionizing electric field has turned off, by at least T_{QB} — in practice post-propagation on much

TABLE III. Energies (in Hartrees) of the occupied orbitals of the neon ground state, in the HF (DF^b) approximation, for non-relativistic all-electron (AE), scalar relativistic effective-core potential (sRECP), and scalar+vector RECP calculations. In all cases, the radial grid extends to $r_{\max} = 400$ Bohr, with a non-uniform spacing of grid points following (II-9).

Orbital	AE ^a	AE*	AE ^b	RECP ^c	sRECP*	RECP*
1s	-32.772 445 5	-31.5391	-32.817 475			
2s	-1.930 390 95	-1.9296	-1.935 847	-1.931 353	-1.9497	-1.9497
2p _{1/2}	-0.850 409 65	-0.850 289	-0.852 829	-0.855 553	-0.845 115	-0.848 401 9
2p _{3/2}	"	"	-0.848 267	-0.848 056	"	-0.843 478 8
ΔE_{s-o}	0	0	4.563×10^{-3}	7.497×10^{-3}	0	4.9231×10^{-3}
Total	-128.547 10	-126.283	-128.691 990	-34.706 149	-34.6807	-34.6807

^a HF limit, Froese Fischer [30]

^b Dirac-Fock values obtained from RCIS [8]

^c Generated from the RECP by Nicklass *et al.* [52] using DIRAC19 [53] with a decontracted aug-cc-pVQZ basis set.

* this work

longer timescales is required. In contrast, using iSURF we can compute the spectrum converged to infinite time directly after the end of the pulse, and for the ultrashort pulse considered here, it is hardly a problem to keep the whole wavefunction in the box, which enables us to use the iSURF method with Coulomb asymptotics (iSURFC) which yields essentially the exact spectrum, within our Ansatz (I-2).

The large resonances are due to the intermediate states $2s 2p^6(^2S) np \ ^1P_1^o$ which decay into $2s^2 2p^5(^2P_j^o) ks, d \ ^1P_1^o$. The precise location of these resonances differ between the AE and RECP calculations, due to the difference in calculated orbital energies (as seen in Table III); the experimental value for the 3p resonance is approximately 24 eV [46, 54]. The centre-of-mass of the resonance lines agree between the scalar RECP and the RECP, since the former is derived from the latter by averaging the spin-orbit part of the potential. The splitting of the lines are approximately 0.1 eV, in agreement with the spin-orbit splitting of the ion ground state. The $J = 3/2$ lines appears at the higher kinetic energy of the photoelectron, since the associated ionization potential is lower. Its strengths are approximately double that of the $J = 1/2$ line, due to the double number of available channels (four vs two). The AE results appear consistently ~ 0.69 eV below the RECP results throughout the Rydberg series, and the energy axis of the upper panel has been shifted to reflect this. The location of the $2s^{-1}$ threshold has been computed in Koopman's approximation, i.e. as the difference of the 2p and 2s orbital energies; the experimental value is 26.9 eV [55], the large discrepancy between theory and experiment is due to the lack of relaxation of the remaining electrons at the CIS level.

Interspersed between the large resonances are two additional series, one broader (corresponding to shorter autoionizing lifetimes) and the other narrower (corresponding to longer lifetimes). These result from the $2s 2p^6(^2S) ns \ ^1S$ and $2s 2p^6(^2S) nd \ ^1D$ series, respectively, which requires two photons to reach. The same symme-

tries are found in the direct channel $2s^2 2p^5(^2P_j^o) k\ell$, for $\ell = p, f$, which also require two photons, which explains why these peaks are comparatively weaker. Although the $2s 2p^6(^2S) ns$ series is unaffected by spin-orbit interaction, the autoionization peaks are split due to the splitting of the intermediate state $2s 2p^6(^2S) n'p$.

E. Spin-polarized photoelectrons in strong fields

As a final example of the accuracy and power of the TD-CIS method, we try to reproduce a recent experiment by Trabert *et al.* [56], where spin-polarized photoelectrons were produced by ionizing xenon using intense circularly polarized light. In accordance with the predictions by Barth and Smirnova [57], a strong connection between the final ion state and the photoelectron spin is observed, leading to high spin polarization of the ATI peaks. Additionally, the spin polarization varies with the ATI peak order, since the tunnelling conditions leading to a certain peak favour the co- and counter-rotating spatial orbitals differently.

The radial grid of Equation (II-9) used when solving the HF problem consists of 40 points with the parameters given in Table I, and $W_{k \max} = 1$ Ha $\implies \rho_{\max} = 0.354$ Bohr gives $I_p^{J=3/2} = 0.446$ Ha, $I_p^{J=1/2} = 0.501$ Ha. This results in a spin-orbit splitting of $\Delta E_{s-o} = 54.5$ mHa = 1.48 eV, which is slightly larger than the experimental value $\Delta E_{s-o}^{\text{exp}} \sim 1.3$ eV. The time propagation is performed on a larger grid of 217 points, where the spacing after the 40th point is constant at $\rho = 0.341$ Bohr, extending to $r_{\max} \gtrsim 70$ Bohr. The t+iSURF matching radius is at $R_s = 41.86$ Bohr. Restricting excitation/ionization to only occur from the 5p electrons (i.e. 6 channels) and including all orbital angular momenta up to $\ell_{\max} = 15$ results in 3072 partial waves [see Equation (II-10)].

The ionizing field is similar to the one used for the experiment; a driving wavelength of $\lambda = 395$ nm, corresponding to a pulse energy of $\hbar\omega = 3.14$ eV, an intensity

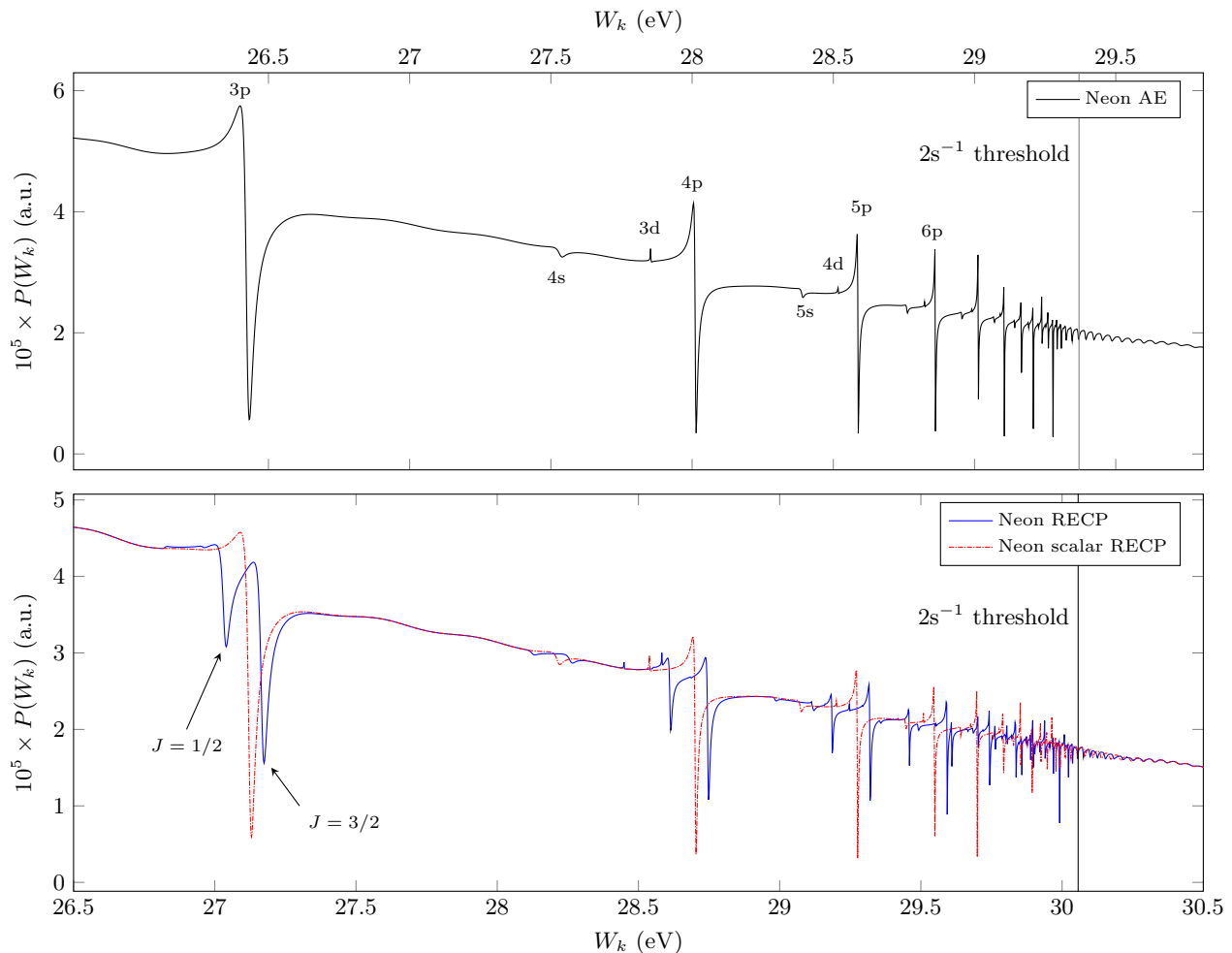


FIG. 7. Photoionization spectrum of neon at the magic angle $\theta = \arctan \sqrt{2}$ with respect to the polarization direction, in the vicinity of the Fano resonances converging to the $2s^{-1}$ threshold, computed using various levels of theory; non-relativistic all-electron (AE) (1s frozen, only 2s, p allowed to ionize) in the upper panel, and in the lower panel, a relativistic effective core potential (RECP) in solid blue, and finally its scalar counterpart in dot-dashed red. The panels have been aligned to the $2s^{-1}$ threshold, see main text.

of $I = 60 \text{ TW/cm}^2$, and (right-handed) circular polarization. The plane of polarization is chosen to be the x - y plane, such that the spin polarization along z is non-zero. The pulse duration was however chosen as $T = 4 \text{ fs}$ instead of the 40 fs of the experiment, since converging the spin polarization for longer pulse durations becomes prohibitively expensive; longer pulse durations necessitate larger orbital angular momenta ℓ_{max} . Additionally, a pulse duration $T = 40 \text{ fs}$ would yield a pulse bandwidth narrower than the typical error in transition energies due to the CIS *Ansatz*. A frequency scan would be required for comparison with the experiment. When the energy errors are within the bandwidth of the shorter pulse, the physical effect can robustly be reproduced, without a parameter scan.

Finally, the photoelectron spectrum was resolved on a momentum grid, with 200 points linearly spaced in energy from 0.01 eV to 15 eV, 20 points along $\theta \in [0, \pi]$ and 41 points along $\phi \in [0, 2\pi]$. Volkov scattering states (i.e.

$t+i\text{SURFV}$) was employed, since the whole wavefunction could not be kept within the computational box. The results are shown in Figure 8; the individual spectra for spin-up and spin-down electrons (angularly integrated), respectively, as well as the energy-resolved spin polarization, computed as

$$S[\%] = 100 \frac{P_\alpha - P_\beta}{P_\alpha + P_\beta}.$$

Also shown are the experimental results by Trabert *et al.* [56], with which the theoretical spin polarization seems to be in satisfactory agreement.

II.5. CONCLUSIONS

We have described an efficient propagator for the time-dependent configuration-interaction singles *Ansatz* spe-

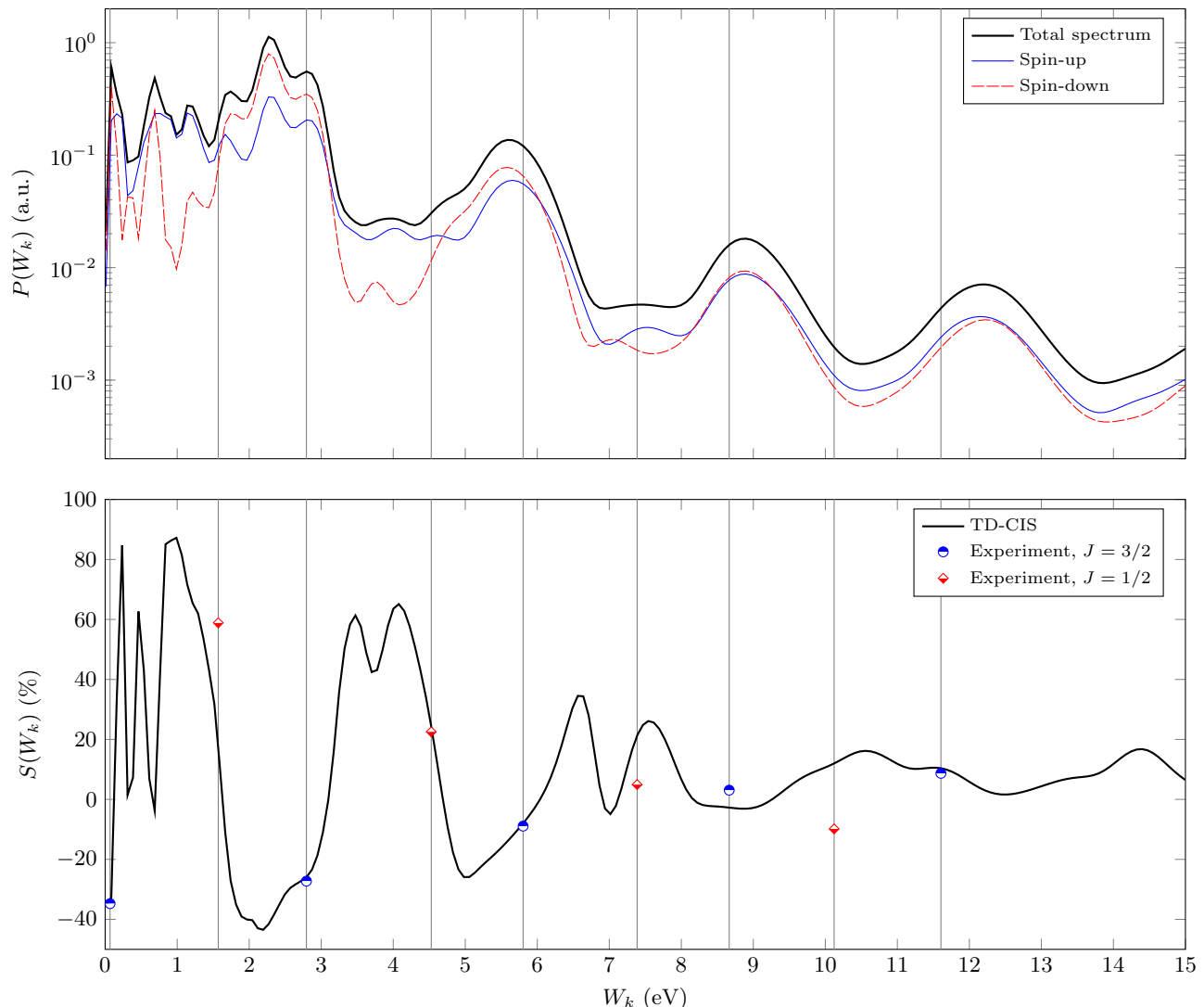


FIG. 8. Spin polarization of photoelectrons emitted during ionization of xenon using a circularly polarized field of $I = 60 \text{ TW/cm}^2$ of $\lambda = 395 \text{ nm}$. The ringing at low energies ($W_k < 1 \text{ eV}$) is an artefact, due to the combination of a small computational box and a Volkov continuum [51]; $R_s \approx 42 \text{ Bohr}$.

cialized to the case of spherical symmetry, and demonstrated its correctness with some simple examples, as well as its ability to compute fine spectral features such as the spin-orbit splitting of the Fano lines in photoionization of neon. We have finally illustrated its capability to *ab initio* faithfully reproduce some of the latest experimental results pertaining to the production of spin-polarized photoelectrons in strong-field processes, an exciting area of research that is only going to grow in the near future.

ACKNOWLEDGMENTS

It is a pleasure to thank Sheehan Olver for the collaboration on quasiarrays and Michael Spanner, Misha Yu. Ivanov, Morten Piibelet, Pranav Singh, Rasmus Henningsson, Ken Schafer, and Sølve Selstø for illuminating

discussions.

SCM is supported by scholarship 185-608 from *Olle Engkvists Stiftelse*. JMD acknowledges support from the *Knut and Alice Wallenberg Foundation* (2017.0104 and 2019.0154), the *Swedish Research Council* (2018-03845) and *Olle Engkvists Stiftelse* (194-0734).

Appendix A: Quasimatrices

As stated in the introduction, the spin-angular degrees of freedom are treated analytically using standard angular momentum algebra. The radial degrees of freedom are described in the language of *quasimatrices* [58], which are objects where the first dimension is formally continuous on the interval $[a, b]$, and the second dimension discrete. Using a notation reminiscent of that of Dirac, a quasi-

matrix can be written as

$$\mathbf{B} = [|1\rangle |2\rangle \dots |n\rangle],$$

where the columns $|i\rangle$ are functions on the interval $[a, b]$, usually chosen to constitute a complete set on this interval in the limit $n \rightarrow \infty$. Any function may thus be expanded as $|f\rangle = \mathbf{B}\mathbf{f}$, where \mathbf{f} is the column vector of expansion coefficients. Similarly, the one-dimensional time-independent Schrödinger equation attains the familiar form of a generalized eigenvalue equation

$$\begin{aligned} \hat{H}|\Psi\rangle &= E|\Psi\rangle \\ \implies \mathbf{B}^\dagger \hat{H} \mathbf{B} \mathbf{c} &= \mathbf{B}^\dagger E \mathbf{B} \mathbf{c} \iff \mathbf{H} \mathbf{c} = E \mathbf{S} \mathbf{c}, \end{aligned}$$

where the matrix representation of the Hamiltonian is given by $H_{ij} = \langle i|\hat{H}|j\rangle$, and the overlap matrix $S_{ij} = \langle i|j\rangle$. In the case $S_{ij} = \delta_{ij}$, we recover the standard eigenvalue problem. The dual vectors $\langle i|$, and hence the dual basis \mathbf{B}^\dagger , are taken to be the complex conjugates of $|i\rangle$ and \mathbf{B} , respectively. In non-Hermitian quantum mechanics, where the left and right vectors in general do not coincide [29], this is strictly speaking an approximation.

The advantage of working with quasimatrices, instead of the matrix representations of the operators directly, is that it becomes easier to integrate different basis sets into the same code base; to solve the HF problem, only the following operations need to be implemented: basis function overlap $\langle i|j\rangle$, scalar functions (e.g. potentials) $\langle i|\hat{V}|j\rangle$, derivatives $\langle i|\partial^{(n)}|j\rangle$, for $n = 1, 2$, and mutual densities $\langle k|i\rangle\langle j|l\rangle$ [corresponding to the function product $h(x) = f(x)g(x)$].

The HF solver underpinning this TD-CIS implementation has been implemented using quasimatrices [59], and thus supports finite-differences of various kinds [40, 60],

as well as finite-elements discrete variable representation [61], and B-splines [62]. However, the time propagator component presently requires diagonal overlap matrices $S_{ij} \sim \delta_{ij}$, diagonal potential matrices, and tridiagonal derivative matrices, for efficiency. An avenue of future improvement could be the implementation of *compact finite-differences* [37, 39, 63], to increase the spatial accuracy and potentially lowering the number of radial grid points required.

Appendix B: Givens rotations

A common theme in the dipole propagators described in section II.3D is the exponentiation of simple 2×2 systems, which can be computed using Givens rotations

$$\mathbf{G}(s, c) \stackrel{\text{def}}{=} \begin{bmatrix} c & s \\ -s^* & c \end{bmatrix}.$$

As an example, the complex-symmetric system

$$\mathbf{A} = -i \begin{bmatrix} 0 & a \\ a & 0 \end{bmatrix}$$

can be exactly exponentiated as $\exp(\mathbf{A}) = \mathbf{G}(\cos a, -i \sin a)$, but we instead opt for the Crank-Nicolson approximation [37]

$$\exp(\mathbf{A}) \approx \frac{1}{1+b^2} \begin{bmatrix} 1-b^2 & -2ib \\ -2ib & 1-b^2 \end{bmatrix} \equiv \frac{\mathbf{G}(1-b^2, -2ib)}{1+b^2}$$

($b \stackrel{\text{def}}{=} \frac{a}{2}$), which is quicker to compute than the trigonometric functions, while still being accurate enough for the small rotation angles a considered.

-
- [1] S. Carlström, M. Spanner, and S. Patchkovskii, General time-dependent configuration-interaction singles I: The molecular case, [2204.09966](#) (2022).
 - [2] D. A. Varshalovich, *Quantum Theory of Angular Momentum: Irreducible Tensors, Spherical Harmonics, Vector Coupling Coefficients, 3nj Symbols* (World Scientific Pub, Singapore Teaneck, NJ, USA, 1988).
 - [3] N. Rohringer, A. Gordon, and R. Santra, Configuration-interaction-based time-dependent orbital approach for *Ab Initio* treatment of electronic dynamics in a strong optical laser field, [Physical Review A](#) **74**, 043420 (2006).
 - [4] N. Rohringer and R. Santra, Multichannel coherence in strong-field ionization, [Physical Review A](#) **79**, 053402 (2009).
 - [5] L. Greenman, P. J. Ho, S. Pabst, E. Kamarchik, D. A. Mazziotti, and R. Santra, Implementation of the time-dependent configuration-interaction singles method for atomic strong-field processes, [Physical Review A](#) **82**, 023406 (2010).
 - [6] J. Harriman, *Theoretical foundations of electron spin resonance* (Academic Press, New York, 1978).
 - [7] M. Dolg and X. Cao, Relativistic pseudopotentials: Their development and scope of applications, [Chemical Reviews](#) **112**, 403 (2011).
 - [8] F. Zapata, J. Vinbladh, A. Ljungdahl, E. Lindroth, and J. M. Dahlström, Relativistic time-dependent configuration-interaction singles method, [Physical Review A](#) **105**, 012802 (2022).
 - [9] P. Indelicato and J. P. Desclaux, Projection operator in the multiconfiguration Dirac-Fock method, [Physica Scripta](#) **T46**, 110 (1993).
 - [10] P. Indelicato, Projection operators in multiconfiguration Dirac-Fock calculations: Application to the ground state of heliumlike ions, [Physical Review A](#) **51**, 1132 (1995).
 - [11] C. F. Fischer and O. Zatsarinny, A B-spline Galerkin method for the Dirac equation, [Computer Physics Communications](#) **180**, 879 (2009).
 - [12] C. G. V. de Walle and P. E. Blöchl, First-principles calculations of hyperfine parameters, [Physical Review B](#) **47**, 4244 (1993).
 - [13] C. J. Pickard and F. Mauri, All-electron magnetic response with pseudopotentials: NMR chemical shifts,

- Physical Review B **63**, 245101 (2001).
- [14] W. A. Goddard, *Ab Initio* pseudopotentials (extending *Ab Initio* QM throughout the periodic table), in *Computational Materials, Chemistry, and Biochemistry: From Bold Initiatives to the Last Mile*, Computational Materials, Chemistry, and Biochemistry: From Bold Initiatives to the Last Mile (Springer International Publishing, 2021) pp. 1049–1053.
- [15] E. V. Beck, S. R. Brozell, J.-P. Blaudeau, L. W. Burggraf, and R. M. Pitzer, Assessment of the accuracy of shape-consistent relativistic effective core potentials using multireference spin-orbit configuration interaction singles and doubles calculations of the ground and low-lying excited states of U^{4+} and U^{5+} , *The Journal of Physical Chemistry A* **113**, 12626 (2009).
- [16] S. O. Odoh and G. Schreckenbach, Performance of relativistic effective core potentials in DFT calculations on actinide compounds, *The Journal of Physical Chemistry A* **114**, 1957 (2009).
- [17] S. Pabst, A. Sytcheva, A. Moulet, A. Wirth, E. Goulielmakis, and R. Santra, Theory of attosecond transient-absorption spectroscopy of krypton for overlapping pump and probe pulses, *Physical Review A* **86**, 063411 (2012).
- [18] G. Strang, On the construction and comparison of difference schemes, *SIAM Journal on Numerical Analysis* **5**, 506 (1968).
- [19] T. Sato, K. L. Ishikawa, I. Březinová, F. Lackner, S. Nagele, and J. Burgdörfer, Time-dependent complete-active-space self-consistent-field method for atoms: Application to high-order harmonic generation, *Physical Review A* **94**, 023405 (2016).
- [20] T. Teramura, T. Sato, and K. L. Ishikawa, Implementation of a gauge-invariant time-dependent configuration-interaction-singles method for three-dimensional atoms, *Physical Review A* **100**, 043402 (2019).
- [21] M. Hochbruck and A. Ostermann, Exponential integrators, *Acta Numerica* **19**, 209 (2010).
- [22] D. E. Manolopoulos, Derivation and reflection properties of a transmission-free absorbing potential, *J. Chem. Phys.* **117**, 9552 (2002).
- [23] U. V. Riss and H.-D. Meyer, Calculation of resonance energies and widths using the complex absorbing potential method, *Journal of Physics B: Atomic, Molecular and Optical Physics* **26**, 4503 (1993).
- [24] U. V. Riss and H.-D. Meyer, The transformative complex absorbing potential method: a bridge between complex absorbing potentials and smooth exterior scaling, *Journal of Physics B: Atomic, Molecular and Optical Physics* **31**, 2279 (1998).
- [25] N. Moiseyev, Derivations of universal exact complex absorption potentials by the generalized complex coordinate method, *Journal of Physics B: Atomic, Molecular and Optical Physics* **31**, 1431 (1998).
- [26] N. Moiseyev, Quantum theory of resonances: calculating energies, widths and cross-sections by complex scaling, *Physics Reports* **302**, 212 (1998).
- [27] R. Santra and L. S. Cederbaum, Non-Hermitian electronic theory and applications to clusters, *Physics Reports* **368**, 1 (2002).
- [28] A. Scrinzi, Infinite-range exterior complex scaling as a perfect absorber in time-dependent problems, *Physical Review A* **81**, 053845 (2010).
- [29] N. Moiseyev, *Non-Hermitian Quantum Mechanics* (Cambridge University Press, Cambridge New York, 2011).
- [30] C. Froese Fischer, *The Hartree–Fock Method for Atoms: A Numerical Approach* (Wiley, New York, 1977).
- [31] C. F. Fischer and W. Guo, Spline algorithms for the Hartree–Fock equation for the helium ground state, *Journal of Computational Physics* **90**, 486 (1990).
- [32] C. W. McCurdy, M. Baertschy, and T. N. Rescigno, Solving the three-body Coulomb breakup problem using exterior complex scaling, *Journal of Physics B: Atomic, Molecular and Optical Physics* **37**, R137 (2004).
- [33] C. W. McCurdy and F. Martín, Implementation of exterior complex scaling in B-splines to solve atomic and molecular collision problems, *Journal of Physics B: Atomic, Molecular and Optical Physics* **37**, 917 (2004).
- [34] M. Wolfsberg, Dipole velocity and dipole length matrix elements in π electron systems and configuration interaction, *The Journal of Chemical Physics* **23**, 793 (1955).
- [35] D. H. Kobe, Gauge-invariant resolution of the controversy over length versus velocity forms of the interaction with electric dipole radiation, *Physical Review A* **19**, 205 (1979).
- [36] K. Ishikawa and T. Sato, A review on *Ab Initio* approaches for multielectron dynamics, *IEEE Journal of Selected Topics in Quantum Electronics* **21**, 8700916 (2015).
- [37] H. G. Muller, An efficient propagation scheme for the time-dependent Schrödinger equation in the velocity gauge, *Laser Physics* **9**, 138 (1999).
- [38] K. J. Schafer, *Numerical methods in strong field physics* (Springer, 2009) pp. 111–145.
- [39] S. Patchkovskii and H. Muller, Simple, accurate, and efficient implementation of 1-electron atomic time-dependent Schrödinger equation in spherical coordinates, *Computer Physics Communications* **199**, 153 (2016).
- [40] J. L. Krause and K. J. Schafer, Control of THz emission from Stark wave packets, *The Journal of Physical Chemistry A* **103**, 10118 (1999).
- [41] V. V. Kolosov, A hydrogen atom in a strong electric field, *Journal of Physics B: Atomic and Molecular Physics* **20**, 2359 (1987).
- [42] J. Rumble, *CRC Handbook of Chemistry and Physics: A Ready-Reference Book of Chemical and Physical Data* (CRC Press/Taylor & Francis Group, Boca Raton, 2021).
- [43] U. D. Jentschura, Resummation of the divergent perturbation series for a hydrogen atom in an electric field, *Physical Review A* **64**, 013403 (2001).
- [44] D. Tannor, *Introduction to Quantum Mechanics: A Time-Dependent Perspective* (University Science Books, Sausalito, Calif, 2007).
- [45] V. Kaufman and L. Minnhagen, Accurate ground-term combinations in Ne I, *Journal of the Optical Society of America* **62**, 92 (1972).
- [46] E. B. Saloman, Wavelengths, energy level classifications, and energy levels for the spectrum of neutral neon, *Journal of Physical and Chemical Reference Data* **33**, 1113 (2004).
- [47] S. Mukamel, *Principles of Nonlinear Optical Spectroscopy* (Oxford University Press, New York, 1995).
- [48] K. Kaufmann, W. Baumeister, and M. Jungen, Universal Gaussian basis sets for an optimum representation of Rydberg and continuum wavefunctions, *Journal of Physics B: Atomic, Molecular and Optical Physics* **22**, 2223 (1989).
- [49] J.-A. You, N. Rohringer, and J. M. Dahlström, Attosecond photoionization dynamics with stimulated core-

- valence transitions, *Physical Review A* **93**, 033413 (2016).
- [50] O. Smirnova, V. S. Yakovlev, and M. Ivanov, Use of electron correlation to make attosecond measurements without attosecond pulses, *Physical Review Letters* **94**, 213001 (2005).
- [51] F. Morales, T. Bredtmann, and S. Patchkovskii, iSURF: a family of infinite-time surface flux methods, *Journal of Physics B: Atomic, Molecular and Optical Physics* **49**, 245001 (2016).
- [52] A. Nicklass, M. Dolg, H. Stoll, and H. Preuss, *Ab Initio* energy-adjusted pseudopotentials for the noble gases Ne through Xe: Calculation of atomic dipole and quadrupole polarizabilities, *The Journal of Chemical Physics* **102**, 8942 (1995).
- [53] A. S. P. Gomes, T. Saue, L. Visscher, H. J. Aa. Jensen, R. Bast, I. A. Aucar, V. Bakken, K. G. Dylla, U. E. S. Dubillard, E. Eliav, E. F. T. Enevoldsen, T. Fleig, O. Fossgaard, E. D. H. L. Halbert, B. Heimlich-Paris, J. H. T. Helgaker, M. Iliaš, S. K. Ch. R. Jacob, S. Komorovský, J. K. L. O. Kullie, C. V. Larsen, H. S. N. Y. S. Lee, M. K. Nayak, G. O. P. Norman, J. Olsen, J. M. H. Olsen, J. K. P. Y. C. Park, M. Pernpointner, K. R. R. di Remigio, P. Salek, B. S. B. Schimmelpfennig, A. Shee, J. Sikkema, J. T. A. J. Thorvaldsen, J. van Stralen, S. V. M. L. Vidal, O. Visser, T. Winther, and S. Yamamoto, *DIRAC19, a relativistic Ab Initio electronic structure program* (2019).
- [54] K. Codling, R. P. Madden, and D. L. Ederer, Resonances in the photo-ionization continuum of Ne I (20–150 eV), *Physical Review* **155**, 26 (1967).
- [55] A. E. Kramida and G. Nave, The Ne II spectrum, *The European Physical Journal D* **39**, 331 (2006).
- [56] D. Trabert, A. Hartung, S. Eckart, F. Trinter, A. Kalinin, M. Schöffler, L. P. H. Schmidt, T. Jahnke, M. Kunitski, and R. Dörner, Spin and angular momentum in strong-field ionization, *Physical Review Letters* **120**, 043202 (2018).
- [57] I. Barth and O. Smirnova, Spin-polarized electrons produced by strong-field ionization, *Physical Review A* **88**, 013401 (2013).
- [58] S. Olver, R. M. Slevinsky, and A. Townsend, Fast algorithms using orthogonal polynomials, *Acta Numerica* **29**, 573 (2020).
- [59] S. Olver, S. Carlström, and T. S. Gutleb, *JuliaApproximation/ContinuumArrays.jl: v0.9.0* (2021).
- [60] S. L. Adler and T. Piran, Relaxation methods for gauge field equilibrium equations, *Reviews of Modern Physics* **56**, 1 (1984).
- [61] T. N. Rescigno and C. W. McCurdy, Numerical grid methods for quantum-mechanical scattering problems, *Physical Review A* **62**, 032706 (2000).
- [62] C. de Boor, *A Practical Guide to Splines: With 32 Figures* (Springer, New York, 2001).
- [63] S. K. Lele, Compact finite difference schemes with spectral-like resolution, *Journal of Computational Physics* **103**, 16 (1992).